Electronic Supplementary Material (ESI) for Nanoscale.
This journal is © The Royal Society of Chemistry 2018

Supplementary information: Nano-SQUIDs with controllable weak links created via current-induced atom migration

Wout Keijers,[1] Xavier D. A. Baumans,[2] Ritika Panghotra,[1] Joseph Lombardo,[2]
Vyacheslav S. Zharinov,[1] Roman B. G. Kramer,[3] Alejandro V. Silhanek,[2] and Joris Van de Vondel[1,*]

[1]*Laboratory of Solid-State Physics and Magnetism, KU Leuven, Celestijnenlaan 200D, box 2414, BE-3001 Leuven, Belgium*
[2]*Experimental Physics of Nanostructured Materials, Q-MAT, CESAM, Université de Liège, B-4000 Sart Tilman, Belgium*
[3]*Univ. Grenoble Alpes, CNRS, Institut Néel, 38000, Grenoble, France*

(Dated: July 27, 2018)

* joris.vandevondel@kuleuven.be

CONTENTS

I. IN SITU OBSERVATION OF ELECTROMIGRATION

Ex-situ investigation of the structural and morphological modifications caused by controlled electromigration (EM) requires delicate mounting-dismounting and reinstallation procedures risking at every step to damage the sample. In addition, this cumbersome approach leaves little freedom to study, in the same device, different stages of the electromigration process. In order to safely track the evolution of the EM, we have developed a compact platform permitting us to carry out electrical transport measurements directly inside a scanning electron microscope (SEM). The in situ observation requires few adjustments and a strict protocol to minimize the risks associated to electrostatic discharges (ESD) and the consequent irreversible damages produced to the samples. Below we briefly review previous succesful attemps to achieve in situ visualization of EM using different techniques followed by a description of the used setup, the mounting procedures and the identification of the drawbacks and possible solutions of the proposed approach.

A. State of the art

The first realizations of in situ SEM imaging of electromigration were reported in the mid 90's on micrometer scale Al and Cu interconnects [20, 21]. This was followed a decade later by studies of the interfacial adhesion [22] and voids migration [23] in Cu. Real time imaging of electromigration at the nanoscale in gold nanowires during the formation of break junctions had to wait until 2007 [24]. Later, studies of voids formation in long Cu nanowires [25] and healing effect when inverting the bias current were evidenced by transmission electron microscopy (TEM) and scanning transmission electron microscopy (STEM) in thin palladium–platinum bridges [26]. Interestingly, in situ observation of EM using Atomic Force Microscopy (AFM) has been recently implemented for the study of nanogaps formation [27] and structural changes [28] in gold nanowires. Both atomic force- and electron beam-based techniques can be regarded as complementary, as the latter is bringing high resolution insights on a two-dimensional level, while the former is capable of furnishing informations about the out-of-plane axis which turns out to be essential to identify hillocks, protrusions, and voids. In terms of lateral resolution, SEM is superior to AFM imaging. Some of these studies have been performed at room temperature [24, 26, 28] and few of them have used a chip heater to explore the EM around room temperature [20–22]. To our knowledge, in situ electromigration using a cryogenic environement have been reported only in [25].

B. Installation and anti-ESD procedure

The in situ visualisation platform consists of a small (length and width 2 cm) polymer sample holder made of a low degassing material and suitable for working under vacuum conditions. This holder is connected to a thin and flexible flat cable bundle of aluminum wires allowing easy installation, good mechanical stability and little vibrations while simultaneously permitting navigation inside the SEM chamber. The flexible flat cable is connected to a make-before-break (MBB) box (designed to protect the sample from ESD) through BNC outputs via two sub-D9 connectors linked by a gender changer as illustrated in Fig. S1.

Manipulation of small conducting samples as those typically employed for EM require particular precautions in order to avoid electrostatic discharges and ensure repetitive successful installations. The adopted protocol is listed below following a chronological order. In a first step, the sample is wirebonded to the electrical contact pads of the holder. At this point, all the connections are short-circuited to the needle of the wirebonder in order to avoid discharges during bonding while the operator remains at the same electrical potential using a wrist strap. In the next step, all pads stay short-circuited but are disconnected from the wirebonder and brought to the SEM chamber. The reference is then connected to the ground and the user can proceed to separation of the platform. To that end, sub-D9 connectors are separated at the level of the gender changer. The section with the MBB box is then connected to the outside of the SEM door, whereas the sample holder and the flexible cable is installed in the chamber and connected to the inside of the SEM door. For particularly delicate samples, use can be made of an ionizer fan during the installation process.

Frequently, unavoidable ESD occur while connecting the instruments. In order to re-route these discharges, the MBB box contains three types of switches. Each BNC output on the MBB box is interrupted by a switch (S1) able to cut the line and isolate the sample from the instruments. In addition, another switch (S2) allows the line to be connected/disconnected to a common reference and to short-circuit them all together. Finally there is a standalone switch (S3) whose role is to connect the common reference to the ground or to leave it floating.

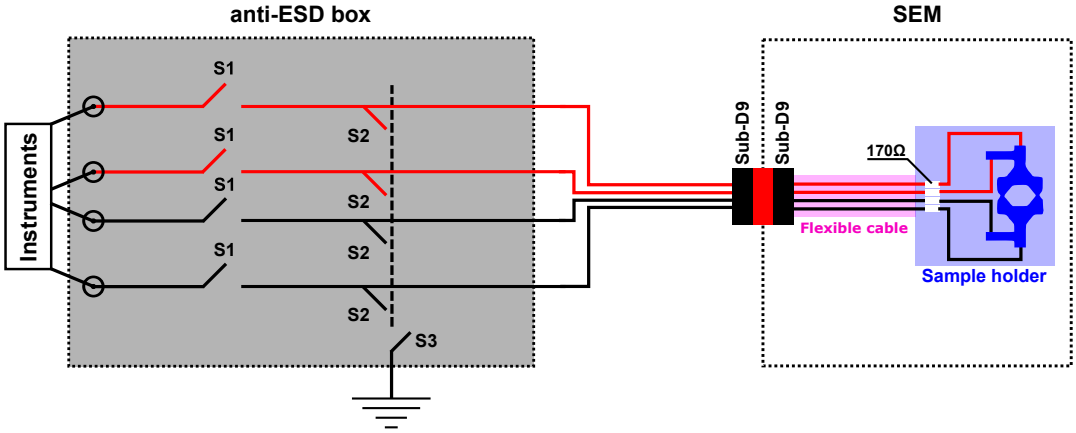

FIG. S1: Schematic representation of the MBB (anti-ESD) box operation in a four-points measurement configuration. Switches S1 are used to isolate instruments from the rest of the experimental setup. Switches S2 are used to connect lines coming from the sample to a common reference (dotted line). Switch S3 allows the common reference to be floating or grounded.

In order to initiate the electrical measurements, all lines are initially disconnected (S1 open) and short-circuited (S2 closed) to the ground (S3 closed). The first step is to connect all lines (close S1) while the sample stays grounded. After this operation, the measurement instruments are connected. This is followed by disconnecting the common reference (open S3). All lines are now still short-circuited but floating. Finally, one can disconnect them from each other (open S2), thus resulting in independent lines connected to measurement devices. An example for a four-points measurement configuration is shown on Fig. S1.

In our case, we used a Raith™ Pionneer Two system for SEM imaging provided with the SmartSEM software (Zeiss™) for saving the image sequence presented in this work.

C. Voltage contrast for visualization of nanogaps

Besides all benefits of in situ visualization of EM, the electrical feedthroughs into the SEM chamber allow, in addition, to better resolve the loci of nanogaps. This is illustrated in Fig. S2. Panel (a) shows a standard SEM image with no external voltage applied, of a sample at the final stage of the EM where a nanogap has been created. The two black arrows indicate places where clear damage is observed although it is not straightforward to discern which one actually exhibits a nanogap percolating through the structure. Indeed, it would require a considerable effort to zoom-in the region of interest to identify a nm-scale gap and follow the fracture through a 200 nm wide region. Fortunately, when an external electrical potential difference is applied to the sample (panels (b) and (c)) a high level of contrast between both sides of the junction makes apparent the loci of the nanogaps in both branches of the SQUID, hence significantly simplifying the task of fracture identification. This phenomenon can be qualitatively understood by considering that on the positive voltage side, secondary electrons (SE) emitted by the nanostructure are retarded [29] whereas on the negative voltage side, SE are repelled from it to the dectector which is translated by a higher signal.

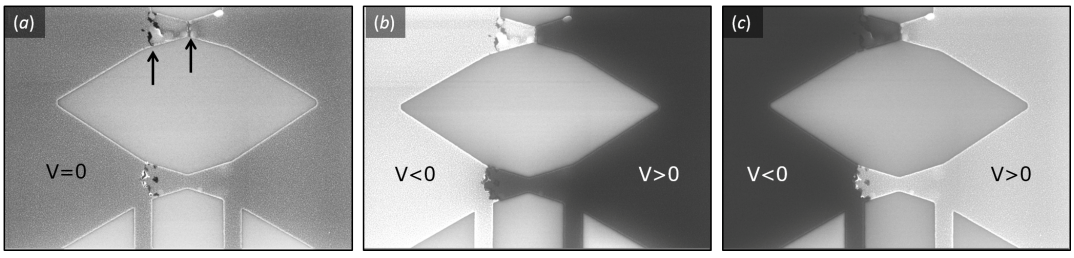

FIG. S2: SEM images of a fully EM sample with nanogaps in both branches of the SQUID for (a) zero applied voltage, and non-zero voltage difference (c-d). The position of the nanogap is clearly determined.

D. Hydrocarbon deposition during in situ imaging

During live inspection a series of snapshots is acquired and the consequent hydrocarbon deposition due to long cumulative exposure time (~ 10 minutes) and beam-energy (10 keV) can be very harmful for the quality and resolution of the images. An example of the consequent loss in resolution can be seen clearly in Fig. 2 a), b) and c) in the main text and Fig. S6 a), b) and c) in the supplementary information. In order to guarantee the non-invasiveness of in situ visualization, it is important to characterize the effects of the hydrocarbon deposition on the EM process.

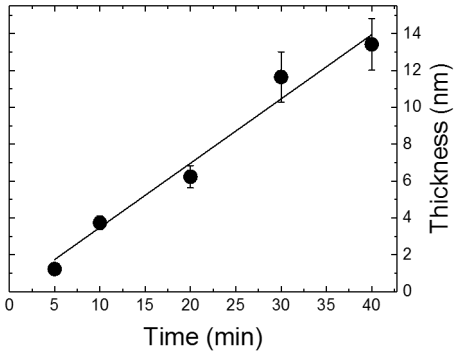

FIG. S3: Thickness of hydrocarbon contamination versus exposure time.

Hydrocarbon contamination are due to the catalysation and polymerization of hydrocarbon compounds present on the sample and in the SEM chamber by the incident electron beam. A review of this problem can be found in Ref. [30, 31]. The deposition rate of such hydrocarbon films can be easily obtained by several exposures for different times under similar conditions as those of the visualization, i.e. electron beam of 10 keV, aperture of 30 μm, beam current ~ 230 pA, and chamber pressure 5.4×10^{-7} mbar. The resulting thickness of the hydrocarbon film is then measured by atomic force microscopy. The contamination layer is not uniform and exhibits a depletion at its center due to immediate cracking of carbon compound during the exposure which are no more allowed to diffuse towards the center of the irradiation area and accumulate at the edges of the scanning window. In the light of this, we can affirm that the amount of contamination remains small compared to the thickness of the studied nano-SQUID's. Indeed, in the case of Fig. 2 in the main text, a sequence of 30 to 40 images have been acquired with a frame time of about 15 seconds per images which correspond to a total exposure time of 10 min. Consequently, the thickness of the hydrocarbon deposition should not exceed 4 nm as inferred from Fig. S3.

Concerning the electrical properties of hydrocarbon contamination, we measured the resistance of a nanogap between two metallic banks made of permalloy (Py) and filled with hydrocarbon compounds. The results are shown in Fig. S4. When the nanogap is not filled with contaminant, the resistance measured is above 10^7 Ω. As the gap is progressively filled by the hydrocarbon, the resistance decreases until saturating at a value close to 10^4 Ω. As long as the sample resistance lies far below the quantum of resistance (1.29×10^4 Ω) the hydrocarbon deposition does not provide a substantial electrical shunt during EM processes [32].

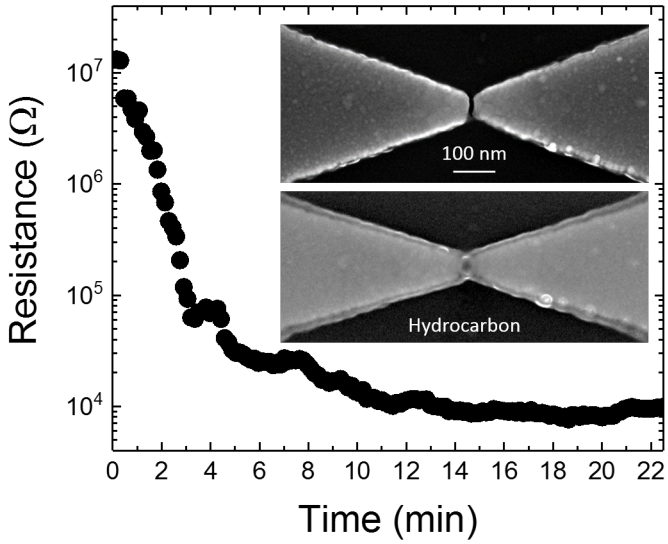

FIG. S4: The main panel shows the time evolution of the resistance through the nanogap as it is filled with hydrocarbon contamination. The upper inset shows the initial nanogap between two permalloy banks formed by electromigration and the lower inset corresponds to a SEM image of the structure after the nanogap has been filled with the contaminant.

The appearance of carbon contamination can be severely limited by overnight pumping of the SEM chamber and decreasing the beam energy. The latter at expenses of lossing in image resolution and contrast. Alternative ways are proposed in Ref. [30].

II. ON THE ELECTROMIGRATION OF PARALLEL WIRES

A. State of the art

The simultaneous electromigration (EM) at room temperature of several nanoconstrictions connected in parallel has been first investigated experimentally by Johnston, Stratchan, and Johnson [33]. These authors recognized the possibility to achieve EM in unison thanks to the naturally balanced power dissipation in each nanowire. In order to ensure that none of the individual nanoconstrictions experience thermal runaway, it turns out to be essential that the inter-nanowire resistance remains lower than the nanoconstriction resistance.

The nano-SQUID shown in Fig.1(a) composed of two shunted variable junction resistances, R and r, can be regarded as the simplest circuit to perform parallel EM. In the initial (virgin) state, uncontrollable and therefore unavoidable factors during the fabrication lead inevitably to an asymmetry between the two legs of the nano-SQUID, i.e. $R > r$. This asymmetry can even be purpously and artifically accentuated via nanofabrication. As a consequence, EM will be initiated preferentially in one of the two constrictions. According to Johnston *et al.* [33], the EM will take place once certain power (or temperature) threshold is reached. Considering that the same voltage drop occurs in each constriction, we obtain $P_R < P_r$ meaning that the constriction with the smallest resistance (i.e. the widest) should undergo EM first. At the start of EM, a rapid increase in the smallest resistance r occurs upon reaching a critical level of power dissipation (and/or critical temperature) at the junction. As r increases due to electromigration, the power P_R dissipated in R must increase at a greater rate than P_r in r in such a way that,

$$\frac{\partial P_r}{\partial r} < \frac{\partial P_R}{\partial r}. \tag{1}$$

When this stability criterion is fulfilled, the EM naturally balances between the two junctions and they can evolve together. Parallel EM has been successfully implemented to generate nanogaps [34] and extended to the case of simple voltage ramps thus permitting to avoid complicated feedback-loop EM [35].

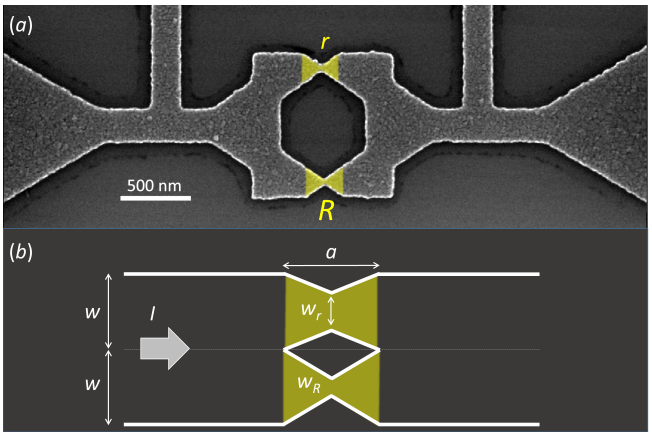

FIG. S5: (a) Al nano-SQUID consisting of two parallel nanoconstrictions with dissimilar resistance values R and r. (b) Sketch of the model discussed in the text.

B. Electrical circuit description of parallel electromigration

It is worth noting that some fundamental questions concerning the sequential evolution of the parallel EM cannot be inferred from the stability criterion described by Eq.1. Indeed, assuming $R > r$, one may wonder in which of the two resistances is the EM going to proceed first. Similarly, we can ask ourselves if in a later stage of the process the EM will alternate between constrictions or advance simultaneously in both of them. In order to experimentally answer these questions, it is essential to be able to carry out in situ visualization of the EM procees. Let us first advance some simple arguments based on the conditions needed to trigger the EM. An alternative scenario to the power triggering the EM process discussed in [33] is to associate the EM with certain current density threshold value. Using Kirchhoff law $rI_r = RI_R$, combined with the current density at the narrowest point of each constriction $J_i = I_i/tw_i$, with $i = r,R$ and t the sample thickness, we obtain $J_R = I_R/w_R = rI_r/Rw_R = rw_rJ_r/Rw_R$. In order to gain further insight, it is imperative to assume a particular constriction geometry as the one depicted in Fig. S5(b) consisting of two constriction in parallel subjected to a total applied current I. The narrowest point of the most (least) resistive constriction is w_R (w_r). The total resistance of each constriction (yellowish section) is given by,

$$r = \frac{a\rho}{t(w-w_r)} ln\frac{w}{w_r}, \qquad R = \frac{a\rho}{t(w-w_R)} ln\frac{w}{w_R}, \tag{2}$$

For this particular yet widely spreaded geometry, we obtain,

$$\frac{J_R}{J_r} = \frac{w_r}{w_R}\frac{w-w_R}{w-w_r}\frac{ln(w/w_r)}{ln(w/w_R)}. \tag{3}$$

The condition $w_r > w_R$ leads to $J_R > J_r$ which suggests that EM should start first at the narrowest constriction, thus contradicting the power threshold model.

In order to discern between the above described scenarios and resolve between these discrepant predictions, it becomes of paramount importance to directly visualize the EM process in parallel junctions. We have performed these measurements in Nb and Al parallel constrictions as shown in Fig. S6. Irrespective of the material, we have verified that EM takes place first at the narrowest constriction. Other effects which are not considered in this analysis are the inhomogeneous current distribution leading to current crowding effects and the granularity of the film.

III. NOTES ON THE ASYMMETRIC MODEL FIT $I_c(\mu_0 H)$

In this section we provide turther details on the fitting of the SQUID's critical current versus field. From these fits three parameters can be extracted: α, β and η. However, due to the correlations between parameters, it is not always

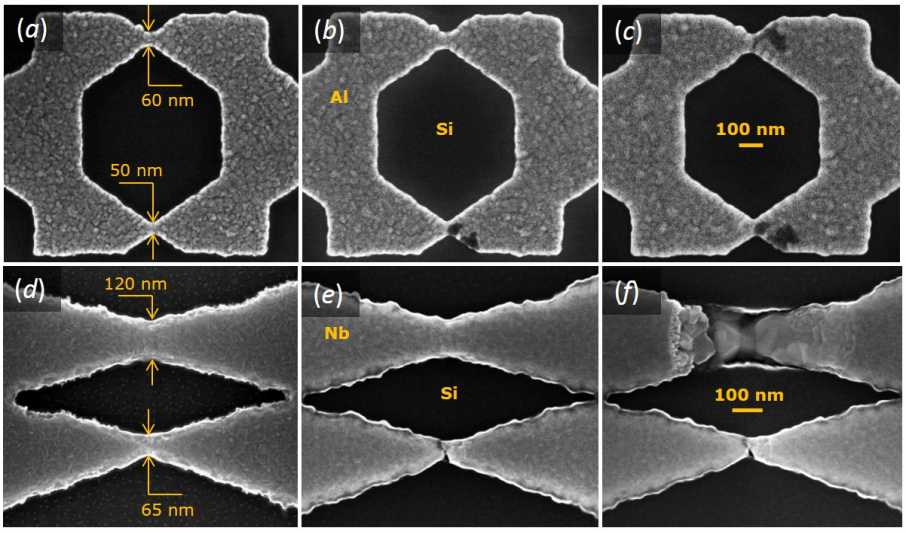

FIG. S6: in situ scanning electron microscopy snapshots of the electromigration process in parallel nanoconstriction of Al (upper row) and Nb (lower row). Panels (a) and (d) show the virgin devices, before electromigration. The asymmetry in the constriction size observed in (a) is unintended, whereas the more pronounced assymetry observed in (d) has been artifially created. Panels (b) and (e) clearly show that EM takes place first at the narrowest constriction for both materials. Further electromigration leads to restribution of current and consequently to EM of the wider contriction as seen in (c) and (f).

possible to have a single well-defined set of parameters fitting the data. Here we discuss the fits $I_c(\mu_0 H)$ of EM 0 (virgin) until EM 6. To reduce the dimensionality of the fitting problem, the period of oscillation and the critical current were directly extracted from the data.

A. Pristine nano-SQUID (EM 0)

First we discuss the fitting of the $I_c(\mu_0 H)$ curve of our virgin SQUID with the asymmetric SQUID model [36] adjusted for the dirty limit Kulik Omel'yanchuk current phase relation (KO-1). The approach we follow is the generally used least-square fit procedure. The best fit is determined by minimizing the sum of squares, weighted by their measurement errors, of the deviation between the data and the fit, i.e. the so-called 'chi-squared' (χ^2). This procedure allows us to find the set of parameters $\{\alpha, \beta, \eta\}$ which minimizes the χ^2-function and results in a curve which gives us the best fit of the data. If we divide the χ^2-function by its degrees of freedom (number of experimental data points minus the number of fitting parameters), we get the reduced χ^2-function, χ^2_{red}

Fig. S7 presents a way to visualize the χ^2_{red} value in three-dimensional parameter space for the data corresponding to the virgin sample. This isosurface represents the values of χ^2_{red} at the minimum of chi-squared plus one ($\min(\chi^2_{red})+1$) and provides an estimate of the error on the fitting parameters [37, 38]. If we take a set of parameters $\{\alpha, \beta, \eta\}$ outside of this surface ($\chi^2_{red} > \min(\chi^2_{red})+1$), the agreement between the data points and the fits is poor. On the contrary, when we take a set $\{\alpha, \beta, \eta\}$ inside of this surface ($\chi^2_{red} < \min(\chi^2_{red})+1$), a good agreement is found. In order to demonstrate this point, a mesh is created in our three-dimensional (α, β, η) parameter space. Each point of this mesh corresponds to a certain set of parameters. Next, we create a box in the parameter space encapsulating the whole isosurface. Within this box we have $\alpha \in [-0.1, 0.15]$, $\beta \in [0.6, 0.85]$ and $\eta \in [-0.1, 0.25]$. Fig. S8 presents the $I_c(\mu_0 H)$ measurment of the virgin sample. A collection of parameter sets inside the isosurface are used to generate the theoretical $I_c(\mu_0 H)$ curves and are presented in transparent blue. These blue curves fit the data well. However, in transparent red, curves generated using sets of parameters outside of the isosurface and inside the previously mentioned box are plotted. These red curves fail to capture the experimental data.

The best fit parameters for the virgin data are $\alpha = 0.01 \pm 0.10$, $\beta = 0.73 \pm 0.09$ and $\eta = 0.07 \pm 0.16$. Note that, using this method of isosurface plotting, we take into account correlations between the parameters and we get an accurate estimate on the error. The conclusions we can formulate from this data are as follows: the arms of the nano-SQUID

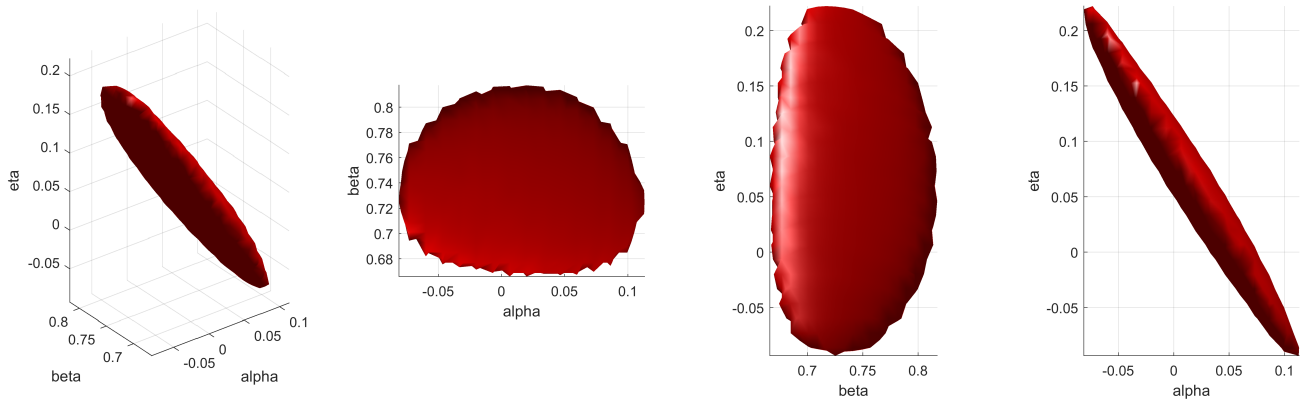

FIG. S7: Isovalues surface in parameter-space at contour value of $\min(\chi^2_{red}) + 1$. (a) 3D isosurface plot in parameter for all three parameters (α, β and η) (b) β vs α (c) η vs β (d) η vs α

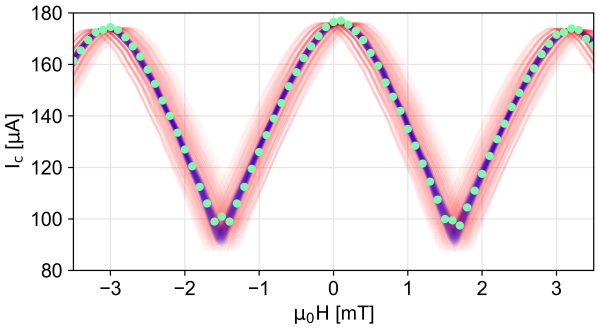

FIG. S8: Sets of parameters $\{\alpha, \beta, \eta\}$ producing curves fitting and not fitting the experimental data of the virgin SQUID. The experimental data is presented as the light green dots. The blue curves are generated using sets of parameters inside the isosurface ($\chi^2_{red} < \min(\chi^2_{red}) + 1$). Red curves are generated using sets of parameters outside the isosurface ($\chi^2_{red} > \min(\chi^2_{red}) + 1$) yet inside a box enclosing the isosurface to keep the parameters reasonably close to the best fitting set. The boundary box taken here is $\alpha \in [-0.1, 0.15]$, $\beta \in [0.6, 0.85]$ and $\eta \in [-0.1, 0.25]$.

are roughly symmetric (the value of α and η and their errors overlap with 0, the symmetric case) and its total loop inductance is $L = 8.5 \pm 1.0$ pH. This value of the inductance matches perfectly with the calculated kinetic inductance of the nano-SQUID.

B. EM 5

Once the EM process has introduced a sizable asymmetry in the device, the fitting deteriorates. For example, the fitting of the $I_c(\mu_0 H)$ curve measured after EM 5 does not produce a well-defined set of parameters fitting the data. Indeed, a high degree of correlation is visible in Fig. S9.

Considering Fig. S9, we conclude that we can not disentangle the η and β_L parameters from our $I_c(\mu_0 H)$ fits anymore. The η and β_L can take vastly different values within the isosurface, i.e. sets of parameters producing curves properly fitting the data. Fig. S10 illustrates that curves generated by sets of parameters inside the isosurface fit nicely, while outside they do not. In contrast to these η and β_L parameters, the α parameter only varies within a reasonable error margin inside this isosurface. As a result, the α parameters provides quantitative information on the asymmetry of the SQUID. We find $\alpha = 0.62 \pm 0.07$.

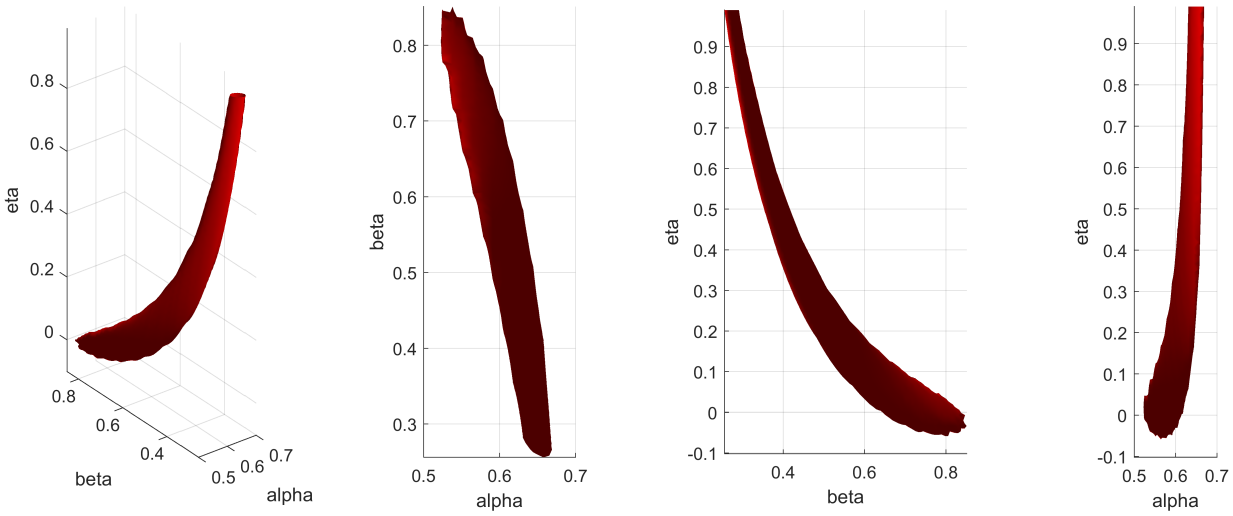

FIG. S9: Isovalues surface in parameter-space at values of $\min(\chi^2_{red}) + 1$ of the fitting of the data after EM5. (a) 3D isovalue plot in χ^2_{red}-space for all three parameters (α, β and η) (b) β vs α (c) η vs β (d) η vs α

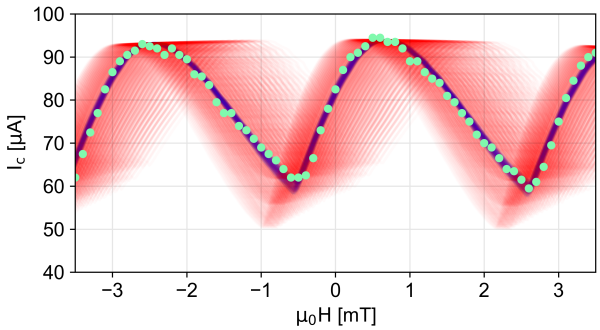

FIG. S10: Sets of parameters $\{\alpha, \beta, \eta\}$ producing curves fitting and not fitting the experimental data after EM5. The experimental data is presented as the light green dots. The blue curves are generated using sets of parameters inside the isosurface ($\chi^2_{red} < \min(\chi^2_{red}) + 1$). Red curves are generated using sets of parameters outside the isosurface ($\chi^2_{red} > \min(\chi^2_{red}) + 1$) yet inside a box enclosing the isosurface to keep the parameters reasonably close to the best fitting set. The boundary box taken here is $\alpha \in [0.5, 0.7]$, $\beta \in [0.2, 0.9]$ and $\eta \in [-0.1, 0.99]$.

C. EM 6

The experimental data measured after EM 6 fitted with the $I_c(\mu_0 H)$ theoretical curve further emphasizes the inability to independently extract η and β_L while still giving a well-defined value for α. Fig. S11 shows the isosurface at $\min(\chi^2_{red}) + 1$ in parameter space of the experimental data measured after the sixth electromigration (EM 6) fitted with the $I_c(\mu_0 H)$ theoretical curve. We find again a well defined value for α ($\alpha = 0.94 \pm 0.01$); the isosurface is only located in a narrow region around a certain value of α. However, similar to the EM 5 fit, β and η are ill-defined. A high correlation between β and η hinders a clear-cut value for each parameter. Fig. S12 displays curves generated using sets of fitting parameters inside the isosurface in blue, outside this isosurface in red. Therefore, no strong claims on the value of β and η can be postulated from these fits.

From the discussion held in this section we can infer that the α parameter is the only fitting parameter from which the evolution on the state of the SQUID after each EM step can unambiguously be determined. In contrast to the α parameter, the fits do not provide univocal values for the β and η parameters. The evolution of the total inductance and the asymmetry of the inductance after electromigration can not be mapped using these fits.

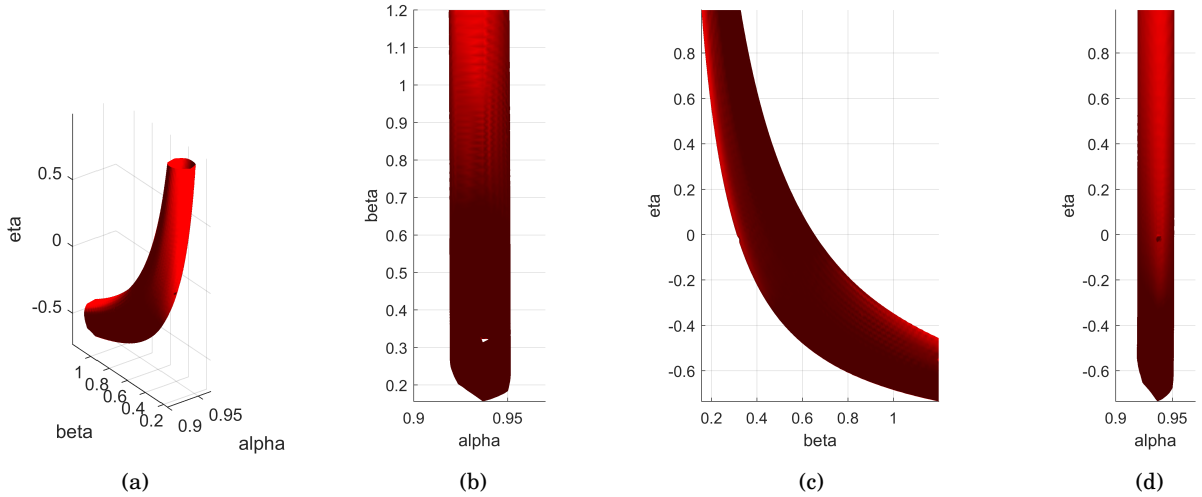

FIG. S11: Isosurface in parameter space at values of min(χ^2_{red}) + 1. (a) 3D isovalue plot in χ^2_{red}-space for all three parameters (α, β and η) (b) β vs α (c) η vs β (d) η vs α

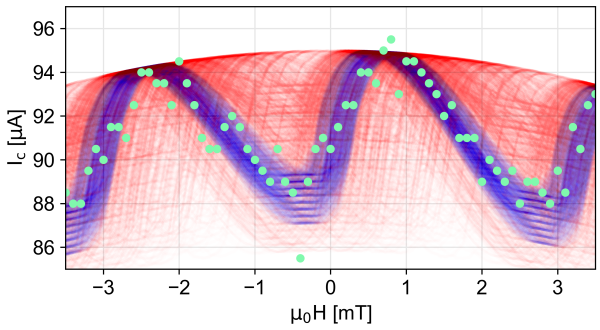

FIG. S12: Sets of parameters $\{\alpha, \beta, \eta\}$ producing curves fitting and not fitting the experimental data measured after EM6. The experimental data is presented as light green dots. The blue curves are generated using sets of parameters inside the isosurface ($\chi^2_{red} < \min(\chi^2_{red}) + 1$). Red curves are generated using sets of parameters outside the isosurface ($\chi^2_{red} > \min(\chi^2_{red}) + 1$) yet inside a box enclosing the isosurface to keep the parameters reasonably close to the best fitting set. The boundary box taken here is $\alpha \in [0.90, 0.99]$, $\beta \in [0.2, 1.2]$ and $\eta \in [-0.7, 0.99]$.

[1] Arzt, E., Kraft, O., Nix, W. D. & Sanchez, J. E. Electromigration failure by shape change of voids in bamboo lines. *Journal of Applied Physics* **76**, 1563–1571 (1994).

[2] Lee, K. L., Hu, C. K. & Tu, K. N. In situ scanning electron microscope comparison studies on electromigration of Cu and Cu(Sn) alloys for advanced chip interconnects. *Journal of Applied Physics* **78**, 4428–4437 (1995).

[3] Lloyd, J. R., Lane, M. W. & Liniger, E. G. Relationship between interfacial adhesion and electromigration in Cu metallization. *IEEE International Integrated Reliability Workshop Final Report* **2002-January**, 32–35 (2002).

[4] Vairagar, A. V. *et al.* In situ observation of electromigration-induced void migration in dual-damascene Cu interconnect structures. *Applied Physics Letters* **85**, 2502–2504 (2004).

[5] Taychatanapat, T., Bolotin, K. I., Kuemmeth, F. & Ralph, D. C. Imaging electromigration during the formation of break junctions. *Nano Letters* **7**, 652–656 (2007).

[6] Huang, Q., Lilley, C. M. & Divan, R. An in situ investigation of electromigration in Cu nanowires. *Nanotechnology* **20** (2009).

[7] Kozlova, T., Rudneva, M. & Zandbergen, H. W. In situ TEM and STEM studies of reversible electromigration in thin palladium-platinum bridges. *Nanotechnology* **24** (2013).

[8] Girod, S. *et al.* Real time atomic force microscopy imaging during nanogap formation by electromigration. *Nanotechnology* **23** (2012).

[9] Yagi, M., Saito, T. & Shirakashi, J.-i. In situ atomic force microscopy imaging of structural changes in metal nanowires during feedback-controlled electromigration. *Journal of Vacuum Science & Technology B, Nanotechnology and Microelectronics: Materials, Processing, Measurement, and Phenomena* **33**, 051806 (2015).

[10] Clarke, D. R. Review: Image contrast in the scanning electron microscope. *Journal of Materials Science* **5**, 689–708 (1970).

[11] Reimer, L. *Scanning Electron Microscopy* (Springer-Verlag, 1998). P. 132.

[12] Egerton, R. F., Li, P. & Malac, M. Radiation damage in the TEM and SEM. *Micron* **35**, 399–409 (2004).

[13] Galvão, D. S., Rodrigues, V., Ugarte, D. & Legoas, S. B. The role of carbon contamination in metallic nanowires. *Materials Research* **7**, 339–342 (2004).

[14] Johnston, D. E., Strachan, D. R. & Johnson, A. T. C. Parallel fabrication of nanogap electrodes. *Nano Letters* **7**, 2774–2777 (2007).

[15] Zhang, H., Thompson, C. V., Stellacci, F. & Thong, J. T. L. Parallel fabrication of polymer-protected nanogaps. *Nanotechnology* **21** (2010).

[16] Johnson, S. L., Hunley, D. P., Sundararajan, A., Johnson, A. T. C. & Strachan, D. R. High-throughput nanogap formation using single ramp feedback control. *IEEE Transactions on Nanotechnology* **10**, 806–809 (2011).

[17] Tesche, C. D., Clarke, J. & Lcli, T. DC SQUID : Noise and Optimization. *J. J Low Temp Phys* **29**, 301–331 (1977).

[18] Taylor, J. R. *An Introduction to Error Analysis: The Study of Uncertainties in Physical Measurements*, vol. 51 (University Science Books, 1983).

[19] Bevington, P. R. & Robinson, D. K. *Data Reduction and Error Analysis for the Physical Sciences, 2nd edn.*, vol. 7 (McGraw-Hill, 1992).

[20] Arzt, E., Kraft, O., Nix, W. D. & Sanchez, J. E. Electromigration failure by shape change of voids in bamboo lines. *Journal of Applied Physics* **76**, 1563–1571 (1994).

[21] Lee, K. L., Hu, C. K. & Tu, K. N. In situ scanning electron microscope comparison studies on electromigration of Cu and Cu(Sn) alloys for advanced chip interconnects. *Journal of Applied Physics* **78**, 4428–4437 (1995).

[22] Lloyd, J. R., Lane, M. W. & Liniger, E. G. Relationship between interfacial adhesion and electromigration in Cu metallization. *IEEE International Integrated Reliability Workshop Final Report* **2002-January**, 32–35 (2002).

[23] Vairagar, A. V. *et al.* In situ observation of electromigration-induced void migration in dual-damascene Cu interconnect structures. *Applied Physics Letters* **85**, 2502–2504 (2004).

[24] Taychatanapat, T., Bolotin, K. I., Kuemmeth, F. & Ralph, D. C. Imaging electromigration during the formation of break junctions. *Nano Letters* **7**, 652–656 (2007).

[25] Huang, Q., Lilley, C. M. & Divan, R. An in situ investigation of electromigration in Cu nanowires. *Nanotechnology* **20** (2009).

[26] Kozlova, T., Rudneva, M. & Zandbergen, H. W. In situ TEM and STEM studies of reversible electromigration in thin palladium-platinum bridges. *Nanotechnology* **24** (2013).

[27] Girod, S. *et al.* Real time atomic force microscopy imaging during nanogap formation by electromigration. *Nanotechnology* **23** (2012).

[28] Yagi, M., Saito, T. & Shirakashi, J.-i. In situ atomic force microscopy imaging of structural changes in metal nanowires during feedback-controlled electromigration. *Journal of Vacuum Science & Technology B, Nanotechnology and Microelectronics: Materials, Processing, Measurement, and Phenomena* **33**, 051806 (2015).

[29] Clarke, D. R. Review: Image contrast in the scanning electron microscope. *Journal of Materials Science* **5**, 689–708 (1970).

[30] Reimer, L. *Scanning Electron Microscopy* (Springer-Verlag, 1998). P. 132.

[31] Egerton, R. F., Li, P. & Malac, M. Radiation damage in the TEM and SEM. *Micron* **35**, 399–409 (2004).

[32] Galvão, D. S., Rodrigues, V., Ugarte, D. & Legoas, S. B. The role of carbon contamination in metallic nanowires. *Materials Research* **7**, 339–342 (2004).

[33] Johnston, D. E., Strachan, D. R. & Johnson, A. T. C. Parallel fabrication of nanogap electrodes. *Nano Letters* **7**, 2774–2777 (2007).

[34] Zhang, H., Thompson, C. V., Stellacci, F. & Thong, J. T. L. Parallel fabrication of polymer-protected nanogaps. *Nanotechnology* **21** (2010).

[35] Johnson, S. L., Hunley, D. P., Sundararajan, A., Johnson, A. T. C. & Strachan, D. R. High-throughput nanogap formation using single ramp feedback control. *IEEE Transactions on Nanotechnology* **10**, 806–809 (2011).
[36] Tesche, C. D., Clarke, J. & Lcli, T. DC SQUID : Noise and Optimization. *J. J Low Temp Phys* **29**, 301–331 (1977).
[37] Taylor, J. R. *An Introduction to Error Analysis: The Study of Uncertainties in Physical Measurements*, vol. 51 (University Science Books, 1983).
[38] Bevington, P. R. & Robinson, D. K. *Data Reduction and Error Analysis for the Physical Sciences, 2nd edn.*, vol. 7 (McGraw-Hill, 1992).